

SN 2015bf: a fast declining type II supernova with flash-ionised signatures

Han Lin,¹ Xiaofeng Wang,^{1,2*} Jujia Zhang,^{3,4,5} Weili Lin,¹ Jun Mo,¹ Alexei V. Filippenko,^{6,7} WeiKang Zheng,⁶ Peter J. Brown,⁸ Danfeng Xiang,¹ Fang Huang,⁹ Yongzhi Cai,¹ Tianmeng Zhang,¹⁰ Xue Li,¹ Liming Rui,¹ Xinghan Zhang,¹ Hanna Sai,¹ Xulin Zhao,¹¹ Melissa L. Graham,¹² I. Shivvers,⁶ G. Halevi,⁶ H. Yuk,¹³ and Thomas G. Brink⁶

¹Physics Department and Tsinghua Center for Astrophysics (THCA), Tsinghua University, Beijing, 100084, China

²Beijing Planetarium, Beijing Academy of Sciences and Technology, Beijing, 100044

³Yunnan Observatories, Chinese Academy of Sciences, Kunming 650011, China

⁴Key Laboratory for the Structure and Evolution of Celestial Objects, Chinese Academy of Sciences, Kunming 650011, China

⁵Center for Astronomical Mega-Science (CAS), 20A Datun Road, Chaoyang District, Beijing, 100012, China

⁶Department of Astronomy, University of California, Berkeley, CA 94720-3411, USA

⁷Miller Senior Fellow, Miller Institute for Basic Research in Science, University of California, Berkeley, CA 94720-3411, USA

⁸George P. and Cynthia Woods Mitchell Institute for Fundamental Physics and Astronomy, Texas A&M University;

Department of Physics and Astronomy, 4242, TAMU, College Station, TX 77843, USA

⁹Department of Astronomy, Shanghai Jiao Tong University, Shanghai 200240, China

¹⁰Key Laboratory of Optical Astronomy, National Astronomical Observatories, Chinese Academy of Sciences, Beijing 100012, China

¹¹School of Science, Tianjin University of Technology, Tianjin 300384, China

¹²DiRAC Institute, Department of Astronomy, University of Washington, Box 351580, Seattle, WA 98195, USA

¹³Homer L. Dodge Department of Physics and Astronomy, The University of Oklahoma, 440 W. Brooks St., Norman, OK 73019, USA

Accepted XXX. Received YYY; in original form ZZZ

ABSTRACT

We present optical and ultraviolet photometry, as well as optical spectra, for the type II supernova (SN) 2015bf. Our observations cover the phases from ~ 2 to ~ 200 d after explosion. The first spectrum is characterised by a blue continuum with a blackbody temperature of $\sim 24,000$ K and flash-ionised emission lines. After about one week, the spectra of SN 2015bf evolve like those of a regular SN II. From the luminosity of the narrow emission component of H α , we deduce that the mass-loss rate is larger than $\sim 3.7 \times 10^{-3} M_{\odot} \text{ yr}^{-1}$. The disappearance of the flash features in the first week after explosion indicates that the circumstellar material is confined within $\sim 6 \times 10^{14}$ cm. Thus, we suggest that the progenitor of SN 2015bf experienced violent mass loss shortly before the supernova explosion. The multiband light curves show that SN 2015bf has a high peak luminosity with an absolute visual magnitude $M_V = -18.11 \pm 0.08$ mag and a fast post-peak decline with a V-band decay of 1.22 ± 0.09 mag within ~ 50 d after maximum light. Moreover, the R-band tail luminosity of SN 2015bf is fainter than that of SNe II with similar peak by 1–2 mag, suggesting a small amount of ^{56}Ni ($\sim 0.009 M_{\odot}$) synthesised during the explosion. Such a low nickel mass indicates that the progenitor of SN 2015bf could be a super-asymptotic-giant-branch star that collapsed owing to electron capture.

Key words: supernovae: general – supernovae: individual (SN 2015bf) – stars: evolution

1 INTRODUCTION

Type II supernovae (SNe II), characterised by abundant hydrogen in their spectra (Minkowski 1941), belong to a class of SNe with diverse observed properties, with Type IIP (plateau) and Type IIL (linear) being the most common subtypes (Barbon et al. 1979). Although SNe IIP and SNe IIL have different light-curve shapes, whether they form two truly distinct classes is still debated (e.g., Arcavi et al. 2012; Anderson et al. 2014; Faran et al. 2014a,b; Sanders et al. 2015). Theoretical studies suggested that the mass of the H envelope can affect the observed properties of SNe II (Litvinova & Nadezhin 1983; Bartunov & Blinnikov 1992; Popov 1993; Morozova et al. 2015; Moriya et al. 2016). Anderson et al. (2014) and

Gutiérrez et al. (2017) showed that the progenitors of fast-declining SNe have a relatively lower-mass H envelope at the time of explosion. The spectra of SNe IIn show prominent narrow or intermediate-width emission lines, which are produced by the interaction between SN ejecta and circumstellar material (CSM; Schlegel 1990; Filippenko 1997).

Recent observations show that narrow emission lines appear not only in SNe IIn, but also in early-time spectra of other subtypes of SNe II. Gal-Yam et al. (2014) referred to spectra showing such emission lines as “flash ionised (FI).” Such FI emission lines are formed as a result of recombination of the outermost CSM, which has been ionised by high-energy photons created during SN shock breakout (Gal-Yam et al. 2014). Khazov et al. (2016) estimated that at least 18% of SNe II show FI signatures in spectra taken at sufficiently early times, and Bruch et al. (2020) suggested an even larger frac-

* E-mail: wang_xf@mail.tsinghua.edu.cn

tion ($> 30\%$ at 95% confidence level) of the SNe II detected in the first year of the Zwicky Transient Facility (ZTF) survey.

It is commonly accepted that SNe II are produced by core collapse and explosion of massive stars ($\geq 8M_{\odot}$; e.g., Smartt 2009). However, the final stages of evolution of massive stars immediately before exploding is still unclear and direct observations are absent. Flash spectra may provide one of the best ways to infer the CSM properties and hence the mass-loss history of the late-phase evolution of the progenitor stars. For example, Yaron et al. (2017) studied the case of SN 2013fs and proposed that the CSM was ejected during the final ~ 1 yr prior to the explosion at an enhanced rate, $\sim 10^{-3} M_{\odot} \text{ yr}^{-1}$. Moreover, the observations of SN 2013fs and SN 2017eaw (Rui et al. 2019) also indicated that pre-SN instabilities may be common among massive stars.

As FI features are usually seen in very early-phase spectra and disappear quickly, detections and studies of such features require rapid observations of SNe II within a few days after explosion; the sample with detections of FI features is thus very limited. In this paper, we present observations and analysis of another SN II (SN 2015bf) with noticeable FI features in early-time spectra, though it was initially classified as a Type IIn supernova. In Section 2, we describe the observations and data reduction. The photometric and spectroscopic evolution of SN 2015bf are presented in Sections 3 and 4, respectively. We discuss the mass-loss history, explosion parameters, and possible progenitor properties in 5. Section 6 summarises our conclusions.

2 OBSERVATIONS AND DATA REDUCTION

2.1 Discovery

SN 2015bf (= PSN J23244903+1516520) was discovered on 2015 December 12.468 (= JD 2,457,368.968; UT dates are used throughout this paper) by Koichi Itagaki using a 0.60 m reflector, with an unfiltered magnitude of ~ 17.3 mag. Its J2000 coordinates are $\alpha = 23^{\text{h}}24^{\text{m}}49.03^{\text{s}}$ and $\delta = 15^{\circ}16'52''.0$, located $4''.0$ west and $20''.0$ north of the centre of host-galaxy NGC 7653 (Fig. 1). SN 2015bf was classified as a young Type IIn SN from a spectrum taken on 2015 December 13.5, which showed narrow emission lines superimposed on a blue continuum (Challis et al. 2015; Zhang et al. 2015). Extensive follow-up observations have been carried out of this object.

The Tully-Fisher distance of 60.1 ± 1.4 Mpc (Springob et al. 2009) from the NASA Extragalactic Database (NED) and a redshift $z = 0.013654$ estimated from H II region emission lines in the host galaxy are adopted throughout this work. The Milky Way reddening is found to be $E(B - V)_{\text{MW}} = 0.059$ mag for SN 2015bf (Schlafly & Finkbeiner 2011), corresponding to a V-band extinction of 0.183 mag assuming the Cardelli et al. (1989) extinction law ($R_V = 3.1$). The equivalent width (EW) of the host-galaxy Na I D absorption feature is 0.62 \AA on day 26.7 (see Fig. 2), suggesting $E(B - V)_{\text{host}} = 0.089$ mag using the empirical relation derived by Turatto et al. (2003). Therefore, the total reddening of SN 2015bf is estimated to be $E(B - V)_{\text{total}} = 0.148$ mag.

2.2 Photometry

After the discovery of SN 2015bf, follow-up optical photometric observations started quickly using several telescopes, including the 80 cm Tsinghua-NAOC Telescope (TNT) at Xinglong Observatory in China (Huang et al. 2012), the 2.4 m Lijiang Telescope (LJT) of

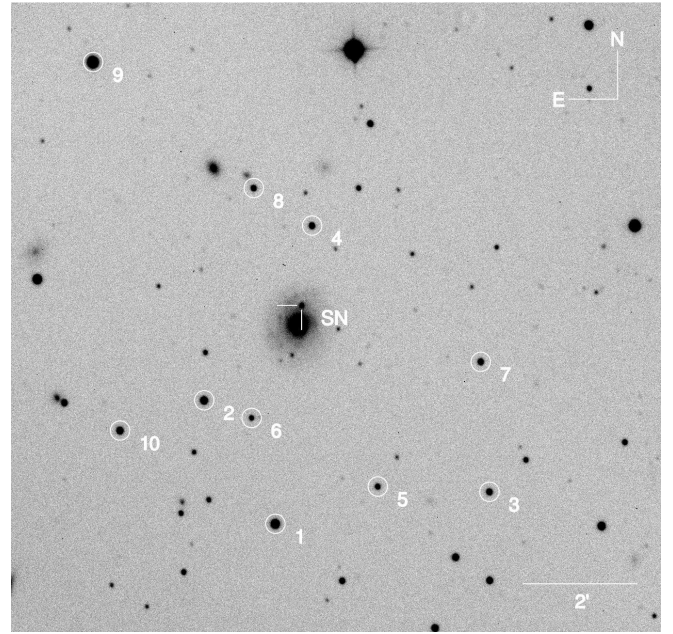


Figure 1. *R*-band image of SN 2015bf in NGC 7653, taken on 2016 Feb. 1 with the Tsinghua-NAOC telescope. North is up and east is to the left. The locations of the supernova and local reference stars are marked by white tick marks and circles, respectively.

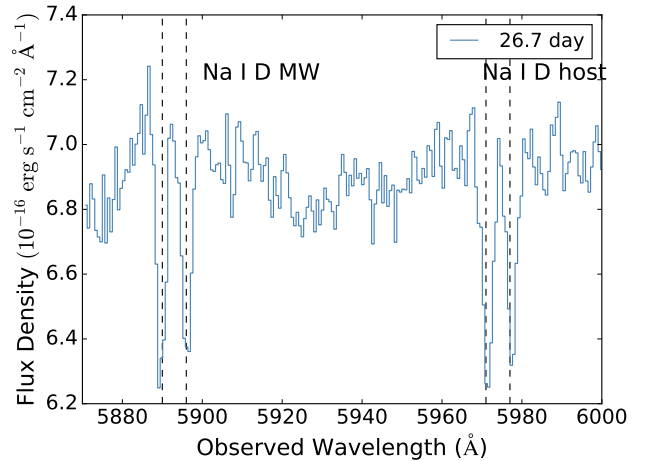


Figure 2. Spectrum taken at $t \approx +26.7$ d shows Na I D absorption from both the Milky Way (MW) and the host galaxy.

Yunnan Astronomical Observatory (YNAO) in China (Fan et al. 2015), the 76 cm Katzman Automatic Imaging Telescope (KAIT) located at Lick Observatory (Richmond et al. 1993; Filippenko et al. 2001), and the Low Resolution Imaging Spectrometer (LRIS; Oke et al. 1995) on the 10 m Keck-I telescope in Hawaii. These data covered the phases from ~ 2 d to ~ 205 d after explosion, and final flux-calibrated magnitudes are presented in Tables A2 and A3.

All CCD images were pre-processed following standard routines, including bias subtraction, flat-field correction, and cosmic-ray removal (Ganeshalingam et al. 2010; Stahl et al. 2019). The template-subtraction technique was applied to the photometry. We performed point-spread-function (PSF) photometry for both the SN and the

reference stars using DAOPHOT (Stetson 1987) or the pipeline Zrutyphot (Mo et al. in prep.) developed for automatic photometry of images collected by TNT and LJT. As there was no template for the R -band image obtained with the Keck-I telescope, we multiplied the total flux in the PSF by a scale factor, treated this as the flux of the SN, and then subtracted this from the total flux. We examined the excess flux to see if its distribution is consistent with the pre-SN image. We tried different scale factors and finally adopted the value 0.45 (see Fig.A1), which gave a measurement of 21.691 ± 0.128 mag. The quoted error are obtained by using scale factors of 0.4 and 0.5, respectively, which can be used as the systematic errors associated with the above method. To test the reliability of such an analysis, we further applied the image subtraction technique by using the pre-SN image from PS1, though it was obtained in r' -band. The resultant value is 21.844 ± 0.086 mag, which is consistent with the above result.

The instrumental magnitudes of the SN were converted into standard Johnson UBV (Johnson et al. 1966) and Kron-Cousins RI (Cousins 1981) using a series of Landolt (Landolt 1992) and PS1 (Chambers et al. 2016; Flewelling et al. 2016; Magnier et al. 2016; Waters et al. 2016) standard stars on a few photometric nights (see Table A1). Apparent magnitudes obtained by KAIT were measured in the KAIT4 natural system. The final results were transformed to the standard system using local calibrators and colour terms for KAIT4 as given in Table 4 of Ganeshalingam et al. (2010), except for the KAIT clear-band data where no reliable colour term is measured owing to the broad response function. We therefore presented the magnitude relative to the reference stars in Landolt R magnitude (Li et al. 2003), which is similar to the KAIT clear band.

SN 2015bf was also observed in the $uvw2$, $uvm2$, $uvw1$, u , b , and v bands using the Ultraviolet/Optical Telescope (UVOT) onboard the *Neil Gehrels Swift Observatory* (Gehrels et al. 2004; Roming et al. 2005). Data reduction followed that of the *Swift* Optical Ultraviolet Supernova Archive (Brown et al. 2009, 2014; Breeveld et al. 2011). A $3''$ or $5''$ aperture was used for the photometry after subtracting the galaxy counts from a template image. The resulting UVOT photometry is listed in Table A4.

2.3 Spectroscopy

15 optical spectra of SN 2015bf were collected using the Xinglong 2.16 m telescope (+BFOSC), the LJT telescope (+YFOSC), the Lick 3 m Shane telescope (+Kast; Miller & Stone 1993), the Keck-II 10 m telescope (+DEIMOS; Faber et al. 2003), and the Keck-I 10 m telescope (+LRIS; Oke et al. 1995). They mostly covered phases from ~ 2 to ~ 50 d after the explosion, though a nebular spectrum was obtained at $t = 205$ d. Details of the spectroscopic observations are listed in Table A5.

All spectra were reduced using standard IRAF pipelines. The procedures included bias and flat-field corrections, cosmic-ray removal, wavelength calibration, and flux calibration. The spectra were corrected for atmospheric extinction using the extinction curves of the local observatories. Telluric absorption was removed through comparison with the standard-star spectra.

3 PHOTOMETRIC PROPERTIES

3.1 Light Curve and Colour Curve

Figure 3 shows the ultraviolet (UV) and optical light curves of SN 2015bf. The last nondetection in archival images was obtained with

KAIT about 2.4 d before the first detection. We thus adopt the mid-point ($t_0 = 2,457,367.77^{+1.2}_{-2.4}$) between the last nondetection and the discovery dates as the estimated explosion time of SN 2015bf, though the upper limit of 17.83 mag in the clear band does not place a tight constraint (the lower limit of explosion time is estimated by a simple power-law (González-Gaitán et al. 2015) fit to the first three data points in V and R bands, see Figure A2, and the upper limit of explosion time is the discovery date).

SN 2015bf reaches the V -band peak with a rise time of ~ 11 d, and the peak is $M_V = -18.11 \pm 0.08$ mag. The R -band peak, $M_R = -18.23 \pm 0.10$ mag, is also consistent with the trend that SNe II with flash-ionised features tend to be luminous (Khazov et al. 2016). After peaking, the V light curve drops by 1.22 ± 0.09 mag within the following ~ 50 d.

In order to further describe the photometric properties of SN 2015bf, we compared the V -band absolute peak magnitude and s_2 parameter (magnitude decline rate per 100 d measured for the second slope of the light curve) of SN 2015bf with those of the SN II sample of Anderson et al. (2014). As shown in Figure 4, SN 2015bf belongs to the brighter and faster declining side of SNe II. Faran et al. (2014b) proposed that SNe IIL seem to decline by more than 0.5 mag from peak brightness by day 50. Based on such a criterion, SN 2015bf should be classified as a SN IIL because of its relatively quick decline (1.03 ± 0.12 mag after peak). Moreover, we noticed that the R -band magnitude at $t \approx 205$ d is fainter than that expected from a linear decline by 2.1 ± 0.13 mag. In Figure 5, we compare the $uvw2$, V , and R light curves of SN 2015bf with those of other well-studied SNe II. One can see that the light-curve properties (i.e., peak brightness and decline rate after maximum) of SN 2015bf are very similar to those of the fast declining SN 2013by and SN 2013ej. If SN 2015bf has the same decline rate during the radioactive tail as SN 2013ej, then the R -band magnitude of SN 2015bf should drop 3.1 ± 0.13 mag from $t \approx 57$ d to $t \approx 100$ d. Valenti et al. (2015) suggested that all SNe IIL exhibit a similar drop in the light curve as SNe IIP, supporting the idea that SNe IIP and SNe IIL share similar underlying physics. Thus, it is possible that SN 2015bf had experienced a significant flux drop before entering the radioactive tail. Nevertheless, Valenti et al. (2015) also showed that some SNe II which decline as fast as SNe IIL do not show significant flux drop, though such sample is rare. This indicates an overall gradual flux decline after the peak cannot be ruled out for SN 2015bf due to the lack of observations between $t \approx 57$ days and $t \approx 205$ days.

The $B - V$ colour curve of SN 2015bf is shown in Figure 6, together with that of SN 1999em, SN2013ej, and SN 2013by. The evolution of its colour curve is similar to that of other SNe II. At early phases, the colour of SN 2015bf is blue. At ~ 10 d, the $B - V$ colour starts to evolve toward the red as the photosphere expands and cools.

3.2 Spectral Energy Distribution

Using the UV and optical photometry, we constructed the spectral energy distribution (SED) and derived the temperatures and radii by applying blackbody fits. Since the phases of *Swift* observations do not match well with those of the *BVRI* observations, we interpolated $uvw2$, $uvw1$, and u data to the epochs when the optical observations are available. However, the *Swift* observations only last for 19 days; after that, we extrapolated the *Swift* observations linearly. We also fit a blackbody to the spectrum at $t = 2.2$ d as it was obtained earlier than the photometry. The SEDs and their blackbody fits are shown in the upper panel of Figure 7, while the evolution of blackbody temperatures and radii is illustrated in the lower panel.

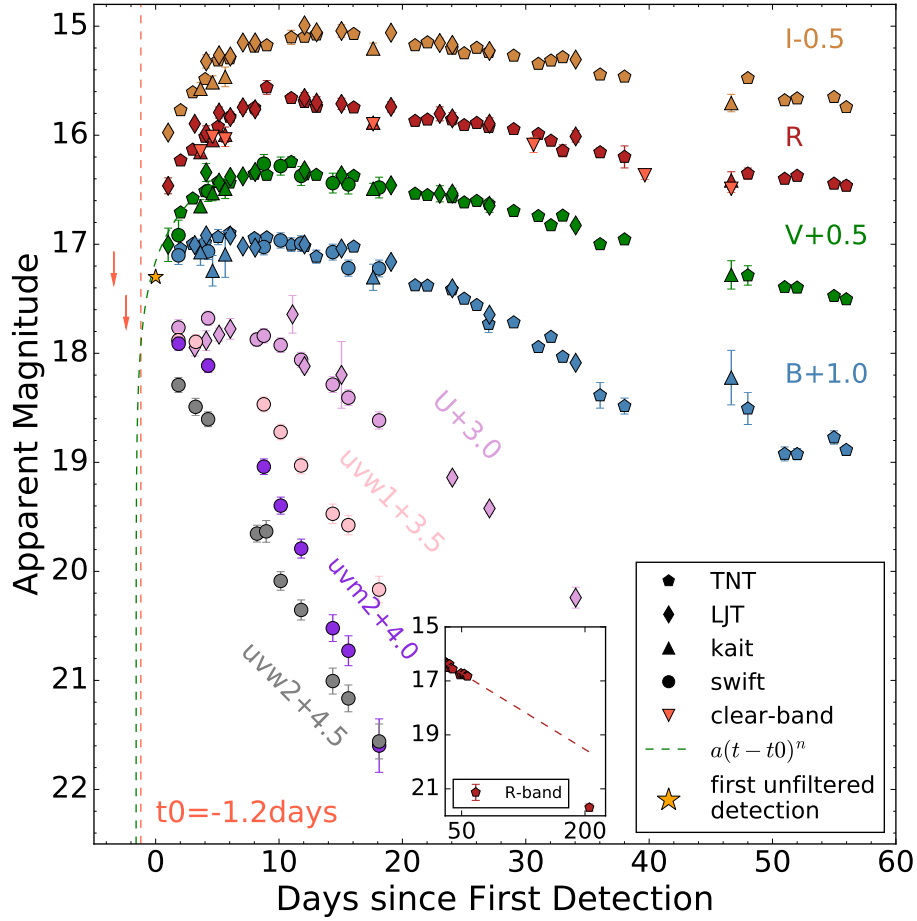


Figure 3. The UV and optical light curves of SN 2015bf. The light curves of different bands have been vertically shifted for clarity. The vertical dashed line marks the explosion date estimate as the midpoint between the last nondetection and discovery. The green dashed line represents the $a(t - t_0)^n$ fits to the V -band magnitudes at early phases. The arrows represent the nondetection upper limits. The inset panel is the R -band light curve at late phases. The red dashed line in the inset is the linear fit for the R data at $t \approx 50$ d after explosion.

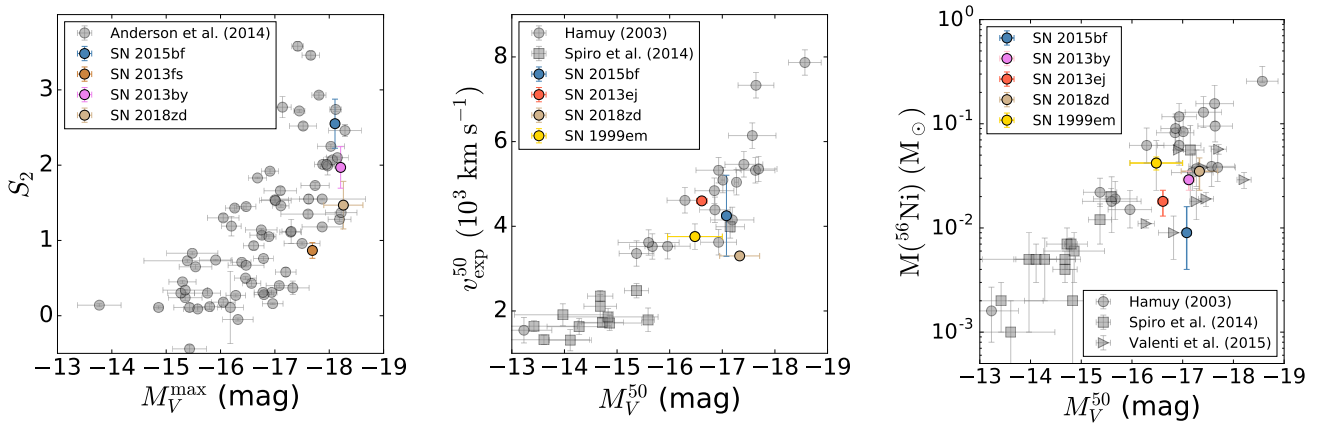


Figure 4. The position of SN 2015bf in the SN II family in terms of various photometric and spectroscopic indicators, including the maximum V -band absolute magnitude (M_V^{\max}), the decline rate of the plateau (s_2), the velocity of Sc II $\lambda 6246$ or Fe II $\lambda 5169$ measured 50 d after explosion (v_{exp}^{50}), the V -band absolute magnitude measured 50 d after explosion (M_V^{50}), and the ^{56}Ni mass. The grey dots represent the sample collected from [Anderson et al. \(2014\)](#), [Hamuy \(2003\)](#), [Spiro et al. \(2014\)](#), and [Valenti et al. \(2015\)](#). SN 1999em, SN 2013ej, SN 2013by, and SN 2018zd are shown for comparison.

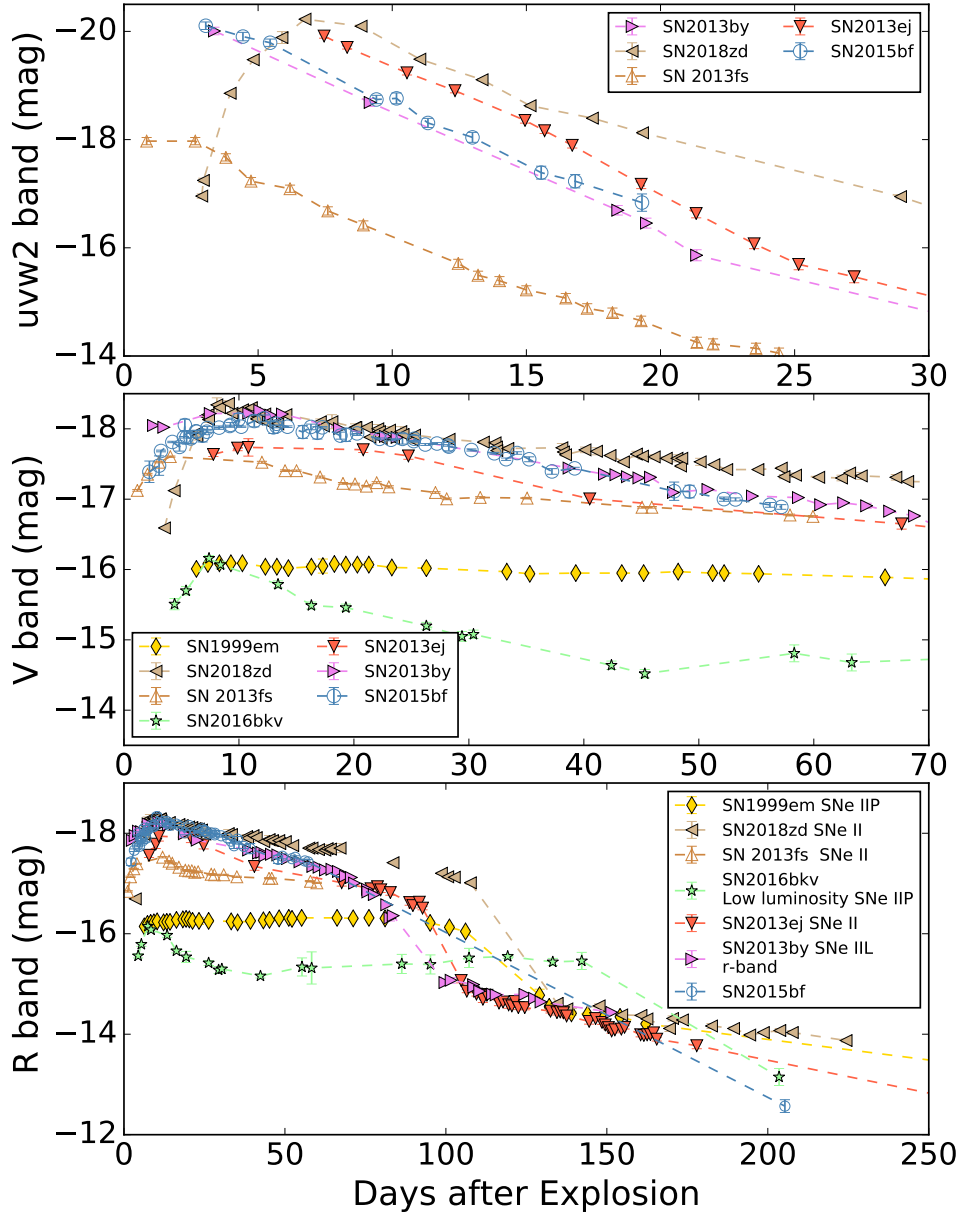


Figure 5. Light-curve comparisons (in absolute magnitude) between SN 2015bf and some well-studied SNe II, including the standard SN IIP 1999em (Hamuy et al. 2001; Leonard et al. 2002; Elmhamdi et al. 2003), the fast-declining SNe II 2013ej (Huang et al. 2015; Dhungana et al. 2016; Yuan et al. 2016) and 2013by (Valenti et al. 2015), and SNe II showing interaction signatures in their spectra such as SN 2013fs (Yaron et al. 2017; Bullivant et al. 2018), SN 2016bkv (Nakaoka et al. 2018; Hosseinzadeh et al. 2018), and SN 2018zd (Zhang et al. 2020).

Hosseinzadeh et al. (2018) noticed a possible temperature rise during the first six days for SN 2016bkv which might be related to the flash ionization of CSM. Such temperature increase was also observed in SN 2018zd (Zhang et al. 2020). For SN 2015bf, we have only one data point before the peak value, which does not allow us to judge its temperature evolution at early phases due to the lack of the UV constraints.

4 OPTICAL SPECTRA

4.1 Evolution of Spectra

The 15 optical spectra of SN 2015bf span from $t = 2.2$ to 205 d after the estimated explosion date. The complete spectral evolution is shown in Figure 8. Figure 9 shows the spectral comparison of SN 2015bf with some representative SNe II at early, photospheric, and nebular phases. The comparison sample includes SN 1998S (Shivers et al. 2015), PTF11iqb (Smith et al. 2015), SN 2013cu (Gal-Yam et al. 2014), SN 2013fs (Yaron et al. 2017), SN 2013ej (Huang et al. 2015; Yuan et al. 2016), SN 2013by (Valenti et al. 2015), SN 2016bkv (Hosseinzadeh et al. 2018), and SN 2018zd (Zhang et al. 2020).

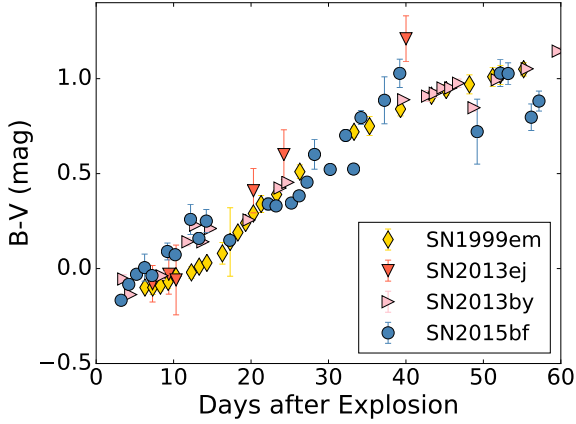


Figure 6. $B - V$ colour evolution of SN 2015bf, compared with that of SN 2013by, SN 2013ej, and SN 1999em.

The first spectrum is characterised by a very blue continuum with prominent emission lines, including $H\alpha$, $H\beta$, $He\ I\ \lambda 4026$, $C\ IV\ \lambda 5801$, and blends of $He\ II\ \lambda 4686$ and $C\ III/N\ III$. The $H\alpha$ feature shows a unique line profile with a narrow core and broad Lorentzian wings, as shown in Figure 10. Such FI emission lines are formed from the recombination of CSM ionised by high-energy photons created by SN shock breakout (Gal-Yam et al. 2014; Khazov et al. 2016). They have been seen in a few other SNe at early times, and their comparisons with SN 2015bf are shown in the upper panel of Figure 9.

The FI features usually exist in very early-time spectra, and they do not last for a long period because the nearby CSM responsible for them is destroyed by the expanding ejecta. In SN 2015bf, we cannot see any emission lines 7.2 d after explosion, except for the faint $H\alpha$ which is likely contributed by the $H\ II$ region. By $t \approx 10$ d, the spectra evolve like those of a regular SN II with broad P-Cygni profiles. As the ejecta expand and the photosphere recedes, we identify absorption features of $Sc\ II$, $Mg\ II$, $Fe\ II$, $Ba\ II$, $Ca\ II$, and $O\ I$; see Figure 8. Comparing with SN 2013ej, SN 2013by, SN 2013fs, and SN 2018zd at the photospheric phase, one can see that these SNe share similar spectral features. Nevertheless, the $H\alpha$ line profile of SN 2015bf has a weaker absorption component in comparison with that of SN 2018zd and SN 2013fs. Previous studies showed that there is a tendency for brighter SNe II with faster post-peak declines to have smaller ratios of absorption to emission in $H\alpha$ (Patat et al. 1994; Schlegel 1996). This can be explained as a result of a less-massive H envelope (Faran et al. 2014b; Gutiérrez et al. 2014) or as an effect of CSM interaction.

Intermediate-width forbidden emission lines characterise nebular-phase spectra of SNe II. For SN 2015bf, we could identify features of $[O\ I]$, $H\alpha$, $Ca\ II$, $Fe\ I$, and $Na\ I$. Compared with SN 2013ej and SN 2018zd at a similar phase, the nebular spectrum of SN 2015bf at $t \approx 205$ d is relatively featureless, with less evident emission lines of $[O\ I]\ \lambda\lambda 6300, 6364$, $Ca\ II\ \lambda 7291$, and $Ca\ II\ \lambda\lambda 8498, 8452$. As the main indicator of the progenitor mass is the $[O\ I]\ \lambda\lambda 6300, 6364$ doublet (Jerkstrand et al. 2012), the weak $[O\ I]$ features of SN 2015bf indicate that its progenitor mass could differ from that of SN 2013ej, although their light-curve properties are similar.

4.2 Ejecta Velocity

For the spectra covering the phases from day 20 to 50 after explosion, the ejecta velocity can be inferred from the absorption minima of the P Cygni profiles. As the absorption feature of $H\alpha$ is not noticeable, we only measured the velocity from the $H\beta$ and $Fe\ II\ \lambda 5169$ lines. The velocity evolution with the best power-law fit is shown in Figure 11. For comparison, we also indicate the power-law fit $v_{Fe} = v_{50}(t/50)^{-0.581 \pm 0.034}$ and $v_{H\beta} = v_{50}(t/50)^{-0.529 \pm 0.027}$ from 23 SNe IIP published by Faran et al. (2014a). The best-fit power-law exponent for $Fe\ II$ is -0.472 ± 0.025 , consistent with the exponent found by Faran et al. (2014a). The photospheric velocity (indicated by $Fe\ II\ \lambda 5169$) measured at $t \approx 50$ d after explosion and the V -band absolute magnitude also follow the luminosity-velocity relation found for SNe IIP (Hamuy 2003). However, the expansion velocity of $H\beta$ declines at a slower rate for SN 2015bf, with a best-fit index of -0.196 ± 0.06 , much smaller than the typical value found for SNe IIP. Such slower velocity evolution for $H\beta$ is consistent with the result found for SNe IIL by Faran et al. (2014b); they explained this as the H line being formed in the outer layers of the ejecta rather than in a gradually exposed H envelope.

5 DISCUSSION

5.1 Presupernova Mass-Loss History

Direct observations of final-stage stellar evolution are very challenging. Flash-ionised features provide opportunities to speculate about the mass-loss history shortly before the SN explosion. For SN 2015bf, considering the ejecta velocity as $\sim 10,000\ km\ s^{-1}$, the disappearance of FI emission lines within the first week after explosion indicates that the CSM should be located at a distance $\lesssim 6 \times 10^{14}\ cm$.

The full width at half-maximum intensity (FWHM) of the $H\alpha$ narrow component in the first spectrum is $\sim 600\ km\ s^{-1}$. If we treat this value as the wind velocity, then the wind can reach the CSM location within 120 d. That means the CSM started to form nearly 120 d before explosion. Since the instrumental FWHM of the first spectrum (measured from the FWHM of the night-sky $O\ I\ \lambda 5577$ emission line) is close to the FWHM of the $H\alpha$ narrow component, the wind velocity inferred from the (FWHM) of the $H\alpha$ narrow component will have large uncertainty. If we instead adopt the wind velocity to be $\sim 100\ km\ s^{-1}$ (as for SN 2013fs), then the CSM started to form ~ 2 yr before the SN explosion.

Following the method described by Ofek et al. (2013) and the relation derived by Osterbrock & Ferland (2006), we also estimate the mass-loss rate based on the luminosity of the narrow $H\alpha$ feature. Assuming a temperature of $\sim 24,000\ K$ (the blackbody temperature of the first spectrum of SN 2015bf), we can then obtain a relation

$$L_{H\alpha} \leq (4.36 \times 10^{39}) \left(\frac{\dot{M}}{10^{-2} M_{\odot} \text{ yr}^{-1}} \right)^2 \left(\frac{v_{\text{wind}}}{500 \text{ km s}^{-1}} \right)^{-2} \left(\frac{r_2 - r_1}{r_1} \right) \left(\frac{r_1}{10^{15} \text{ cm}} \right)^{-1} \text{ erg s}^{-1}, \quad (1)$$

where r_1 and r_2 represent the lower and upper limits of the $H\alpha$ -emitting region, respectively. Here we adopt $r_1 \approx 2.9 \times 10^{14}\ cm$ (the blackbody radius of the first spectrum of SN 2015bf) and $r_2 \approx 6 \times 10^{14}\ cm$. According to the flux of the narrow component of $H\alpha$ ($3.6 \times 10^{-15}\ \text{erg s}^{-1}\ \text{cm}^{-2}$) and adopting a distance of 60.1 Mpc, we derive the $H\alpha$ luminosity as $L_{H\alpha} = 1.56 \times 10^{39}\ \text{erg s}^{-1}$. This luminosity suggests that the mass-loss rate should be larger than $3.7 \times 10^{-3} M_{\odot} \text{ yr}^{-1}$. Such a value is much larger than the typical mass-loss rate of 10^{-6} – $10^{-5} M_{\odot} \text{ yr}^{-1}$ for red supergiants (RSGs) (Smith 2014). Since the flux of $H\alpha$ is enhanced by the host-galaxy

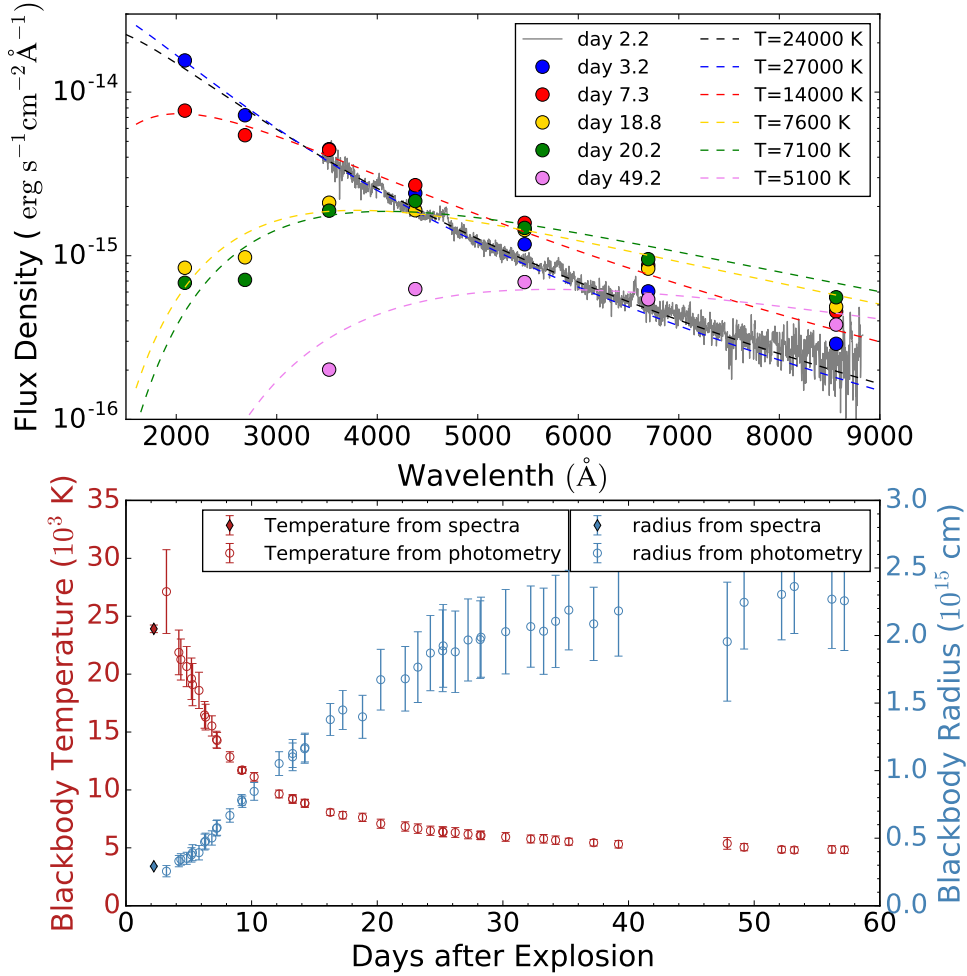


Figure 7. *Upper panel:* SED of SN 2015bf at selected phases. The dashed lines are blackbody fits to the observations. *Lower panel:* Evolution of the blackbody temperature and radius of SN 2015bf.

H II region (see Fig. 10), the true luminosity of H α should be slightly lower, $< 1.56 \times 10^{39} \text{ erg s}^{-1}$. However, the order of magnitude $10^{-3} M_{\odot} \text{ yr}^{-1}$ is consistent with the mass-loss rate of other SNe II, such as SN 2013fs ($\sim 10^{-3} M_{\odot} \text{ yr}^{-1}$; Yaron et al. 2017). Therefore, we consider the derived mass-loss rate of SN 2015bf to be reliable, and we propose that the progenitor of SN 2015bf experienced violent mass loss shortly before exploding.

Khazov et al. (2016) suggested that all of their FI events peak more luminous than $M_R = -17.6$ mag and have SN IIL-like initial decline after the peak. Moreover, they suggested that more luminous SNe tend to maintain higher temperatures during their early-time evolution. SN 2015bf is such an example favouring the above arguments. Morozova et al. (2017) showed that the multiband light curves of SNe IIL can be well fitted by ordinary RSGs surrounded by dense CSM produced a few months or years before the SN explosion. Hillier & Dessart (2019) also proposed that increasing the mass of the CSM will lead to featureless spectra at early phases and weak H α absorption during the recombination phase, which is seen in SN 2015bf. Considering the high peak luminosity, the fast-declining light curve, the blue featureless spectra at early phases, the weak H α absorption in the photospheric phase, and a compact CSM environment, interaction between ejecta and CSM may play an important role in modifying the observed light curves and spectra of SN 2015bf.

5.2 Bolometric Light Curve and Explosion Parameters

The bolometric luminosity of SN 2015bf was derived by integrating the SED from near-infrared through optical emission. Flux outside the wavelength range of photometric coverage was extrapolated based on a blackbody spectrum. Figure 12 displays the bolometric light curve of SN 2015bf. The bolometric light curves of SN 1999em, SN 2013ej, SN 2013by, and SN 2018zd produced by the same method are also shown for comparison. Similar to SN 2013by and SN 2018zd, SN 2015bf has a relatively higher bolometric peak ($L_{\text{max}} = 1.16 \times 10^{43} \text{ erg s}^{-1}$), which is ~ 8 times the peak luminosity of SN 1999em.

Assuming the progenitor of SN 2015bf is an RSG, we can estimate explosion parameters and properties of the progenitor based on empirical relations. Morozova et al. (2016) provide a relation between the g -band rise time and the radius at the time of explosion for SNe II, as they found that the properties of the light curve at early phases depend mainly on the progenitor radius. Using their relation, we can calculate the progenitor radius of SN 2015bf. The g magnitudes of SN 2015bf were converted from B and V data using the relation of Jester et al. (2005). The rise time in g was estimated as $8.5^{+2.4}_{-1.2}$ d, corresponding to a radius of $677^{+241}_{-115} R_{\odot}$.

Litvinova & Nadezhin (1985) connected the mass of the ejecta, the progenitor radius, and the explosion energy to the plateau dura-

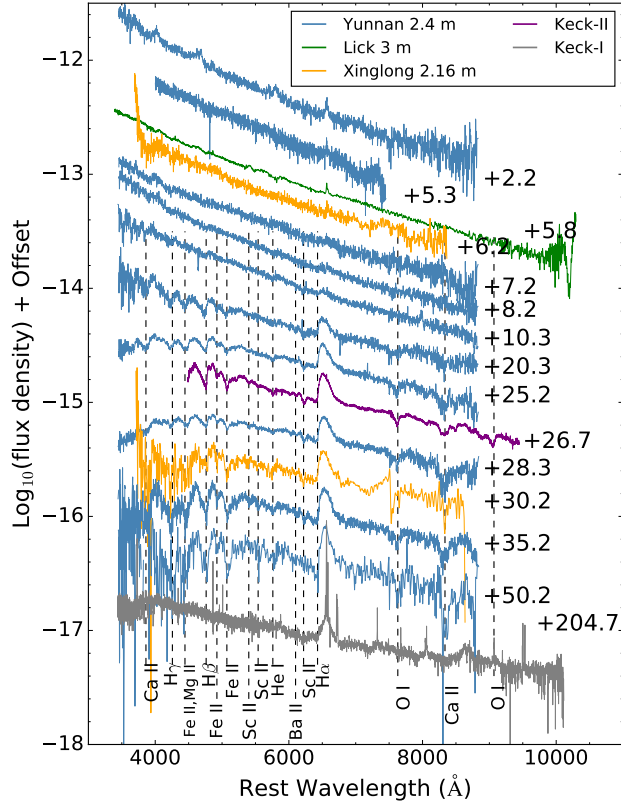


Figure 8. Optical spectra of SN 2015bf, shifted vertically for clarity. All of the spectra have been corrected for host-galaxy and Milky Way extinction. The numbers on the right side mark the epochs of the spectra in days after the explosion. The continuum of the spectra on days +5.3, +20.3, +25.2, and +28.3 has been adjusted with the broadband *UBVRI* photometry at similar phases.

tion, the absolute *V* magnitude, and the photosphere velocity at the mid-plateau epoch. Using their Equation (3), we derived the plateau duration as 56^{+10}_{-14} d. With this plateau duration, we derive the explosion energy to be $(0.35 \pm 0.17) \times 10^{51}$ erg s $^{-1}$ and the ejecta mass to be $3.05^{+2.15}_{-1.72} M_{\odot}$ using their Equations (1) and (2).

5.3 Faint Tail and Electron-Capture Supernova?

As seen in the lower panel of Figure 5, SN 2015bf has a low luminosity in the nebular phase. The *R* magnitude at $t \approx 205$ d after explosion drops by ~ 5 mag compared with the magnitude measured at $t \approx 50$ d after explosion. Although having a similar peak luminosity, the *R* magnitude of SN 2015bf at $t \approx 205$ d is 1.5 ± 0.13 mag fainter than that of SN 2018zd. Its tail luminosity is even fainter than that of SN 2016bkv, whose peak magnitude is much fainter than that of SN 2015bf.

Based on the *R*-band magnitude, we estimated that the luminosity of SN 2015bf at $t \approx 205$ d is only 0.25 ± 0.08 times that of SN 2018zd (the lower and upper limits are estimated when the scale factor is adopted as 0.3 and 0.6, respectively; see Fig. A1). Following the second equation of Hamuy (2003), we estimated the nickel mass of SN 2015bf to be $0.009^{+0.007}_{-0.005} M_{\odot}$. (The lower and upper errors are 3σ uncertainty). As seen in the right panel of Fig. 4, SN 2015bf seems to have less nickel mass compared with other SNe II with similar *V*-band absolute magnitude measured 50 days after

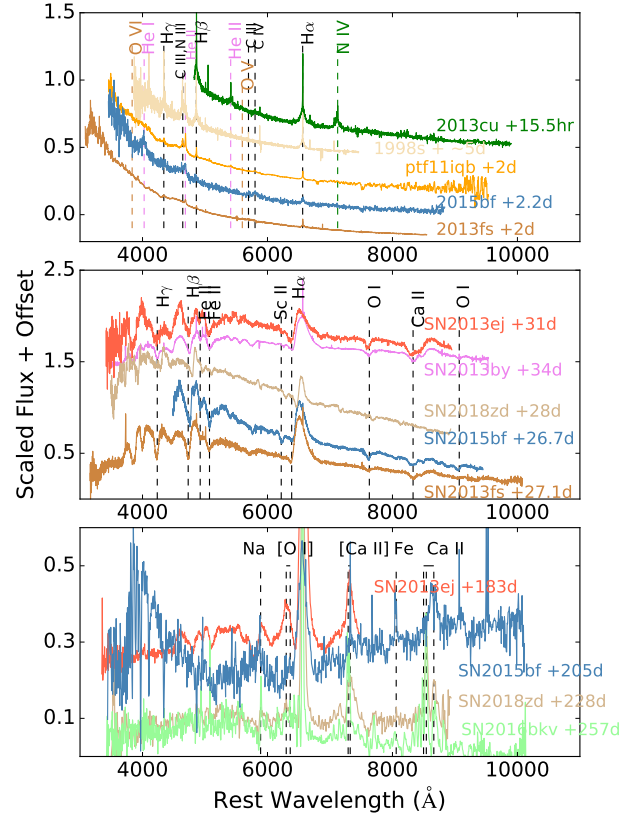


Figure 9. Spectral comparisons of SN 2015bf with SN 1998S (Shivvers et al. 2015), PTF11qib (Smith et al. 2015), SN 2013cu (Gal-Yam et al. 2014), SN2013fs (Yaron et al. 2017), SN 2013ej (Huang et al. 2015; Yuan et al. 2016), SN 2013by (Valenti et al. 2015), SN 2016bkv (Hosseinzadeh et al. 2018), and SN 2018zd (Zhang et al. 2020) at early, photospheric, and nebular phases (top to bottom panels). A blackbody continuum ($T = 7500$ K) has been subtracted from the nebular spectrum of SN 2015bf; narrow emission lines of $H\alpha$, $[N II] \lambda\lambda 6548, 6583$, $[O II] \lambda 3727$, and $[O III] \lambda\lambda 4959, 5007$ from the host galaxy were also removed.

explosion. The equation (2) of Hamuy (2003) assumes that all the gamma rays due to $^{56}\text{Co} \rightarrow ^{56}\text{Fe}$ are fully trapped. For most SNe IIP, this is a reasonable assumption as the decay rates on the tail are consistent with the value for full trapping. For SN 2015bf, we can not conclude whether all the gamma rays are fully trapped as we only have one data point at late times. If not, the nickel mass may be underestimated.

Electron-capture supernovae (Nomoto et al. 1982) are predicted to produce such a small amount of nickel mass ($< 0.015 M_{\odot}$) (Kittaura et al. 2006). Moreover, the progenitors of electron-capture SNe should explode within the CSM environment created by the super-asymptotic-giant-branch (AGB) wind (Moriya et al. 2014). SNe IIn-P (SNe IIn with plateau phase as seen in SNe IIP (Smith 2017)) have been suggested to be related to electron-capture SNe because of their low nickel mass (Sollerman et al. 1998; Kankare et al. 2012; Mauerhan et al. 2013). We noticed that SN 2015bf share similarities with SNe IIn-P. It was initially classified as a SN IIn because of its narrow emission lines. The UV peak absolute magnitude of SN 2015bf ($M_{uvw2} \approx -20$ mag) is also located at the faint end of SNe IIn (Pritchard et al. 2014). Moreover, SN 2015bf possibly suffered a flux drop before entering the radioactive decay phase. Thus, given the massive CSM environment and small amount of synthesised nickel

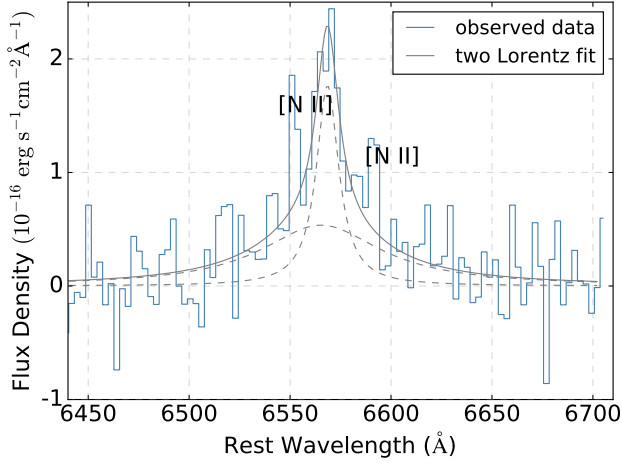


Figure 10. The $H\alpha$ line profile in the spectrum of SN 2015bf, taken at $t \approx 2.2$ d. The grey dashed lines are the Lorentzian fits for the narrow and broad components of the $H\alpha$ line profile. The narrow emission features on both sides of $H\alpha$ are [N II] lines from the host galaxy.

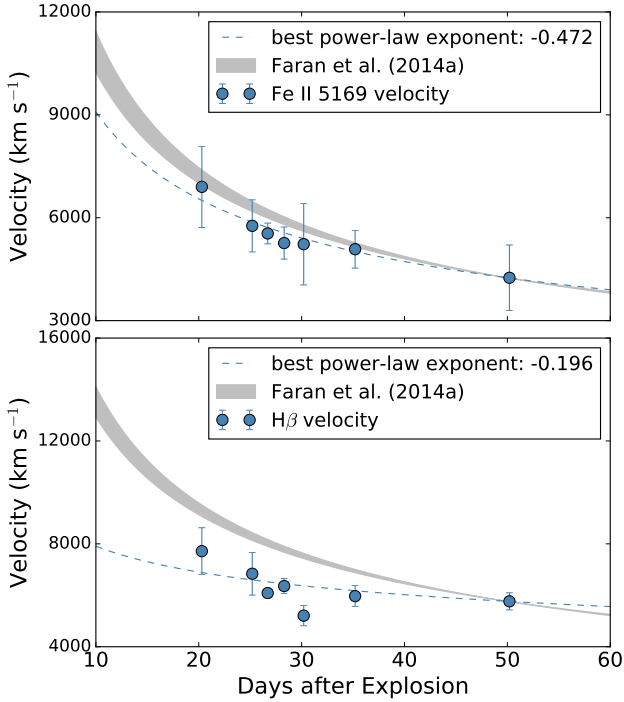


Figure 11. The velocity evolution of $H\beta$ and $Fe\ II\ \lambda 5169$. The blue dashed lines represent the power-law fit for the $H\beta$ and $Fe\ II$ velocities. The grey shaded area represents the power-law fit for SNe IIP from Faran et al. (2014a).

mass, the electron-capture-triggered explosion of a super-AGB star could be a possible scenario for SN 2015bf.

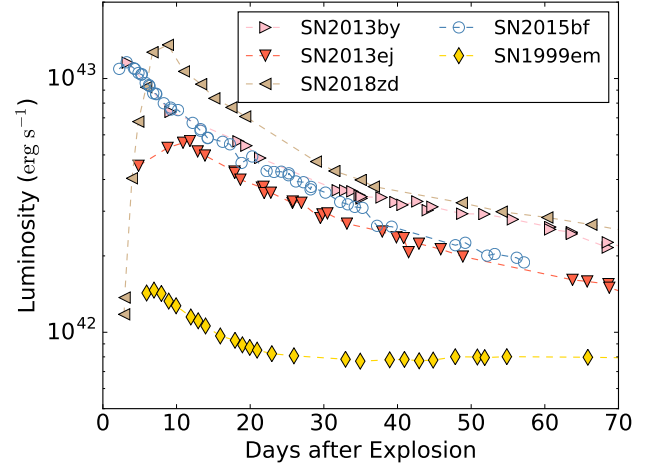


Figure 12. Bolometric light curve of SN 2015bf, compared with those of other well-studied SNe II.

6 CONCLUSIONS

In this work, we present UV and optical observations of SN 2015bf. Our data cover the phase from +2 d to +205 d after the SN explosion. The light curves of SN 2015bf show a higher peak luminosity and a faster post-peak decline rate. Its light curve evolution within ~ 60 days is similar with SN 2013by. It is possible that SN 2015bf suffered a significant flux drop when entering the radioactive tail, but we can not confirm this due to the lack of late-time photometric observations. The photospheric-phase spectra of SN 2015bf, with weak absorption of $H\alpha$ and slow velocity evolution of $H\beta$, are overall more similar to those of SNe IIL.

Moreover, observations of SN 2015bf enrich the SN sample with flash-ionised features at early phases. The spectrum colored obtained at $t \approx 2$ d shows a blue continuum with strong FI emission lines, including $H\alpha$, $H\beta$, He II, and C IV lines. Such FI features only lasted for about a week. Based on these features, one can speculate that the CSM was formed shortly before explosion at an enhanced mass-loss rate of $3.7 \times 10^{-3} M_{\odot} \text{ yr}^{-1}$. Assuming the tail of SN 2015bf is powered only by the radioactive decay of ^{56}Co and all the gamma rays are fully trapped, we estimated the nickel mass of SN 2015bf as $\sim 0.009 M_{\odot}$ from its late-phase luminosity. Such a low nickel mass as well as dusty circumstellar environment, indicate that SN 2015bf could originate from an electron-capture explosion of a super-AGB star.

ACKNOWLEDGEMENTS

We acknowledge the support of the staff of the Lijiang 2.4 m and Xinglong 2.16 m/80 cm telescopes. This work is supported by the National Natural Science Foundation of China (NSFC grants 11633002, 12033002 and 11761141001) and the National Program on Key Research and Development Project (grant 2016YFA0400803). This work is also partially supported by the scholar Program of Beijing Academy of Science and Technology (DZ: BS202002) and the Strategic Priority Research Program of the Chinese Academy of Sciences, Grant No. XDB23040100. J. Zhang is supported by the NSFC (grant 11773067), by the Youth Innovation Promotion Association of the CAS (grant 2018081), and by the Ten Thousand Talents Program of Yunnan for Top-notch Youth Tal-

ents. This work was partially supported by the Open Project Program of the Key Laboratory of Optical Astronomy, National Astronomical Observatories, Chinese Academy of Sciences. The LJT is jointly operated and administrated by Yunnan Observatories and the Center for Astronomical Mega-Science (CAS). Funding for the LJT has been provided by Chinese Academy of Sciences and the Peoples Government of Yunnan Province.

This work is based in part on observations with the twin Keck 10 m telescopes on Maunakea, Hawaii. We are grateful to the staff at the Keck Observatory for their assistance, and we extend special thanks to those of Hawaiian ancestry on whose sacred mountain we are privileged to be guests. The W. M. Keck Observatory is operated as a scientific partnership among the California Institute of Technology, the University of California, and NASA; it was made possible by the generous financial support of the W. M. Keck Foundation. We thank S. Bradley Cenko and Daniel Perley for assistance with Keck spectral reductions. This work made use of *Swift*/UVOT data reduced by P. J. Brown and released in the *Swift* Optical/Ultraviolet Supernova Archive (SOUSA). SOUSA is supported by NASA's Astrophysics Data Analysis Program through grant NNX13AF35G.

A.V.F.'s supernova group is grateful for financial assistance from the TABASGO Foundation, the Christopher R. Redlich Fund, and the Miller Institute for Basic Research in Science (U.C. Berkeley). KAIT and its ongoing operation were made possible by donations from Sun Microsystems, Inc., the Hewlett-Packard Company, Auto-Scope Corporation, the Lick Observatory, the US National Science Foundation, the University of California, the Sylvia & Jim Katzman Foundation, and the TABASGO Foundation. We thank the staff at Lick Observatory for their support. Research at Lick Observatory is partially supported by a generous gift from Google.

Software: IRAF (Tody 1986, 1993), Zrutyphot (Mo et al. in prep.), SExtractor (Bertin & Arnouts 1996), DAOPHOT (Stetson 1987)

DATA AVAILABILITY

The data underlying this article are available in the article and in its online supplementary material. We upload both the original spectra of SN 2015bf and the spectra used in Fig. 8 (corrected for redshift, host-galaxy extinction and Milky Way extinction, some spectra are also adjusted with the photometry) to the online supplementary material.

REFERENCES

- Anderson J. P., et al., 2014, *ApJ*, **786**, 67
- Arcavi I., et al., 2012, *ApJ*, **756**, L30
- Barbon R., Ciatti F., Rosino L., 1979, *A&A*, **72**, 287
- Bartunov O. S., Blinnikov S. I., 1992, *Soviet Astronomy Letters*, **18**, 43
- Bertin E., Arnouts S., 1996, *A&AS*, **117**, 393
- Breeveld A. A., Landsman W., Holland S. T., Roming P., Kuin N. P. M., Page M. J., 2011, in McEnery J. E., Racusin J. L., Gehrels N., eds, *American Institute of Physics Conference Series Vol. 1358, Gamma Ray Bursts 2010*. pp 373–376 ([arXiv:1102.4717](https://arxiv.org/abs/1102.4717)), [doi:10.1063/1.3621807](https://doi.org/10.1063/1.3621807)
- Brown P. J., et al., 2009, *AJ*, **137**, 4517
- Brown P. J., Breeveld A. A., Holland S., Kuin P., Pritchard T., 2014, *Ap&SS*, **354**, 89
- Bruch R. J., et al., 2020, *arXiv e-prints*, [p. arXiv:2008.09986](https://arxiv.org/abs/2008.09986)
- Bullivant C., et al., 2018, *MNRAS*, **476**, 1497
- Cardelli J. A., Clayton G. C., Mathis J. S., 1989, *ApJ*, **345**, 245
- Challis P., Johnson S., Kirshner R., Falco E., Berlind P., Prieto J. L., Stanek K. Z., 2015, *The Astronomer's Telegram*, **8410**, 1
- Chambers K. C., et al., 2016, *arXiv e-prints*, [p. arXiv:1612.05560](https://arxiv.org/abs/1612.05560)
- Cousins A. W. J., 1981, *South African Astronomical Observatory Circular*, **6**, 4
- Dhungana G., et al., 2016, *ApJ*, **822**, 6
- Elmhamdi A., et al., 2003, *MNRAS*, **338**, 939
- Faber S. M., et al., 2003, in Iye M., Moorwood A. F. M., eds, *Society of Photo-Optical Instrumentation Engineers (SPIE) Conference Series Vol. 4841, Proc. SPIE*. pp 1657–1669, [doi:10.1117/12.460346](https://doi.org/10.1117/12.460346)
- Fan Y.-F., Bai J.-M., Zhang J.-J., Wang C.-J., Chang L., Xin Y.-X., Zhang R.-L., 2015, *Research in Astronomy and Astrophysics*, **15**, 918
- Faran T., et al., 2014a, *MNRAS*, **442**, 844
- Faran T., et al., 2014b, *MNRAS*, **445**, 554
- Filippenko A. V., 1997, *ARA&A*, **35**, 309
- Filippenko A. V., Li W. D., Treffers R. R., Modjaz M., 2001, in Paczynski B., Chen W.-P., Lemme C., eds, *Astronomical Society of the Pacific Conference Series Vol. 246, IAU Colloq. 183: Small Telescope Astronomy on Global Scales*. p. 121
- Flewelling H. A., et al., 2016, *arXiv e-prints*, [p. arXiv:1612.05243](https://arxiv.org/abs/1612.05243)
- Gal-Yam A., et al., 2014, *Nature*, **509**, 471
- Ganeshalingam M., et al., 2010, *ApJS*, **190**, 418
- Gehrels N., et al., 2004, *ApJ*, **611**, 1005
- González-Gaitán S., et al., 2015, *MNRAS*, **451**, 2212
- Gutiérrez C. P., et al., 2014, *ApJ*, **786**, L15
- Gutiérrez C. P., et al., 2017, *ApJ*, **850**, 90
- Hamuy M., 2003, *ApJ*, **582**, 905
- Hamuy M., et al., 2001, *ApJ*, **558**, 615
- Hillier D. J., Dessart L., 2019, *A&A*, **631**, A8
- Hosseinzadeh G., et al., 2018, *ApJ*, **861**, 63
- Huang F., Li J.-Z., Wang X.-F., Shang R.-C., Zhang T.-M., Hu J.-Y., Qiu Y.-L., Jiang X.-J., 2012, *Research in Astronomy and Astrophysics*, **12**, 1585
- Huang F., et al., 2015, *ApJ*, **807**, 59
- Jerkstrand A., Fransson C., Maguire K., Smartt S., Ergon M., Spyromilio J., 2012, *A&A*, **546**, A28
- Jester S., et al., 2005, *AJ*, **130**, 873
- Johnson H. L., Mitchell R. I., Iriarte B., Wisniewski W. Z., 1966, *Communications of the Lunar and Planetary Laboratory*, **4**, 99
- Kankare E., et al., 2012, *MNRAS*, **424**, 855
- Khazov D., et al., 2016, *ApJ*, **818**, 3
- Kitaura F. S., Janka H. T., Hillebrandt W., 2006, *A&A*, **450**, 345
- Landolt A. U., 1992, *AJ*, **104**, 372
- Leonard D. C., et al., 2002, *PASP*, **114**, 35
- Li W., Filippenko A. V., Chornock R., Jha S., 2003, *PASP*, **115**, 844
- Litvinova I. I., Nadezhin D. K., 1983, *Ap&SS*, **89**, 89
- Litvinova I. Y., Nadezhin D. K., 1985, *Soviet Astronomy Letters*, **11**, 145
- Magnier E. A., et al., 2016, *arXiv e-prints*, [p. arXiv:1612.05242](https://arxiv.org/abs/1612.05242)
- Mauerhan J. C., et al., 2013, *MNRAS*, **431**, 2599
- Miller J., Stone R., 1993, *Lick Observatory Technical Reports*, [pp 66\(Santa Cruz, CA: Lick Obs.\)](https://arxiv.org/abs/1612.05242)
- Minkowski R., 1941, *PASP*, **53**, 224
- Moriya T. J., Tominaga N., Langer N., Nomoto K., Blinnikov S. I., Sorokina E. I., 2014, *A&A*, **569**, A57
- Moriya T. J., Pruzhinskaya M. V., Ergon M., Blinnikov S. I., 2016, *MNRAS*, **455**, 423
- Morozova V., Piro A. L., Renzo M., Ott C. D., Clausen D., Couch S. M., Ellis J., Roberts L. F., 2015, *ApJ*, **814**, 63
- Morozova V., Piro A. L., Renzo M., Ott C. D., 2016, *ApJ*, **829**, 109
- Morozova V., Piro A. L., Valenti S., 2017, *ApJ*, **838**, 28
- Nakaoka T., et al., 2018, *ApJ*, **859**, 78
- Nomoto K., Sparks W. M., Fesen R. A., Gull T. R., Miyaji S., Sugimoto D., 1982, *Nature*, **299**, 803
- Ofek E. O., Lin L., Kouveliotou C., Younes G., Göğüş E., Kasliwal M. M., Cao Y., 2013, *ApJ*, **768**, 47
- Oke J. B., et al., 1995, *PASP*, **107**, 375
- Osterbrock D. E., Ferland G. J., 2006, *Astrophysics of gaseous nebulae and active galactic nuclei*
- Patat F., Barbon R., Cappellaro E., Turatto M., 1994, *A&A*, **282**, 731
- Popov D. V., 1993, *ApJ*, **414**, 712

- Pritchard T. A., Roming P. W. A., Brown P. J., Bayless A. J., Frey L. H., 2014, [ApJ](#), **787**, 157
- Richmond M., Treffers R. R., Filippenko A. V., 1993, [PASP](#), **105**, 1164
- Roming P. W. A., et al., 2005, [Space Sci. Rev.](#), **120**, 95
- Rui L., et al., 2019, [MNRAS](#), **485**, 1990
- Sanders N. E., et al., 2015, [ApJ](#), **799**, 208
- Schlafly E. F., Finkbeiner D. P., 2011, [ApJ](#), **737**, 103
- Schlegel E. M., 1990, [MNRAS](#), **244**, 269
- Schlegel E. M., 1996, [AJ](#), **111**, 1660
- Shivvers I., Groh J. H., Mauerhan J. C., Fox O. D., Leonard D. C., Filippenko A. V., 2015, [ApJ](#), **806**, 213
- Smartt S. J., 2009, [ARA&A](#), **47**, 63
- Smith N., 2014, [ARA&A](#), **52**, 487
- Smith N., 2017, Interacting Supernovae: Types II_n and Ib_n. p. 403, [doi:10.1007/978-3-319-21846-5_38](#)
- Smith N., et al., 2015, [MNRAS](#), **449**, 1876
- Sollerman J., Cumming R. J., Lundqvist P., 1998, [ApJ](#), **493**, 933
- Spiro S., et al., 2014, [MNRAS](#), **439**, 2873
- Springob C. M., Masters K. L., Haynes M. P., Giovanelli R., Marinoni C., 2009, [ApJS](#), **182**, 474
- Stahl B. E., et al., 2019, [MNRAS](#), **490**, 3882
- Stetson P. B., 1987, [PASP](#), **99**, 191
- Tody D., 1986, in Crawford D. L., ed., Society of Photo-Optical Instrumentation Engineers (SPIE) Conference Series Vol. 627, Proc. SPIE. p. 733, [doi:10.1117/12.968154](#)
- Tody D., 1993, in Hanisch R. J., Brissenden R. J. V., Barnes J., eds, Astronomical Society of the Pacific Conference Series Vol. 52, Astronomical Data Analysis Software and Systems II. p. 173
- Turatto M., Benetti S., Cappellaro E., 2003, in Hillebrandt W., Leibundgut B., eds, From Twilight to Highlight: The Physics of Supernovae. p. 200 ([arXiv:astro-ph/0211219](#)), [doi:10.1007/10828549_26](#)
- Valenti S., et al., 2015, [MNRAS](#), **448**, 2608
- Waters C. Z., et al., 2016, arXiv e-prints, p. [arXiv:1612.05245](#)
- Yaron O., et al., 2017, [Nature Physics](#), **13**, 510
- Yuan F., et al., 2016, [MNRAS](#), **461**, 2003
- Zhang J., Wang X., Zhang K., 2015, The Astronomer’s Telegram, **8412**, 1
- Zhang J., et al., 2020, [MNRAS](#), **498**, 84

APPENDIX A:

This paper has been typeset from a \LaTeX file prepared by the author.

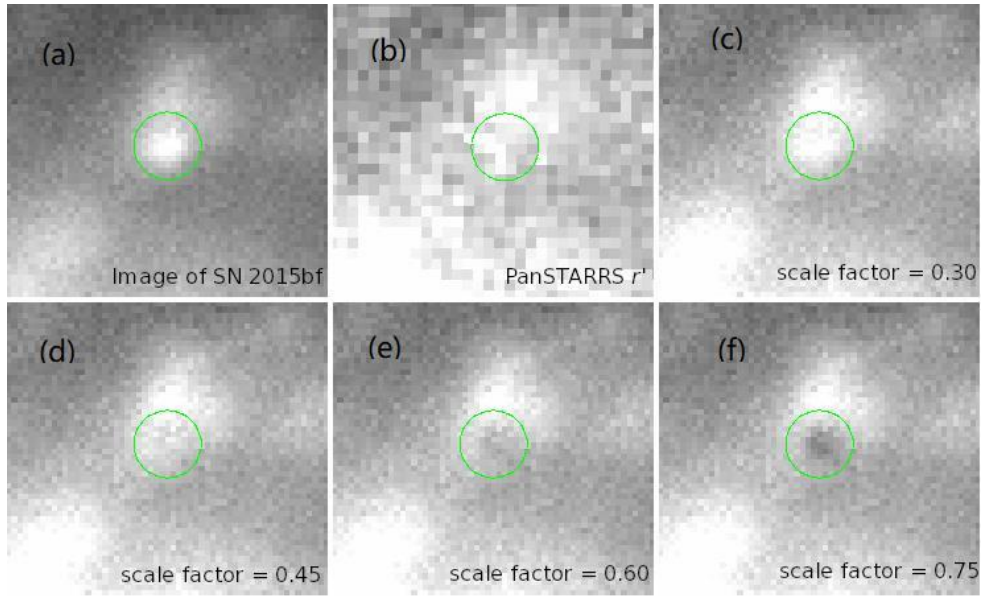


Figure A1. (a): The R -band image of SN 2015bf obtained at $t \approx 205$ d with LRIS on the Keck-I telescope. SN 2015bf is marked by a green circle. (b): r' -band Pre-SN image from PS1. Panels (c), (d), (e) and (f) represent the excess/galaxy flux from which the SN flux has already been subtracted (created by multiplying the total flux in the PSF by a scale factor); see Section 2.2. After comparing with the flux at the SN location from the PS1 pre-SN image, we finally adopt a value of 0.45 for the scale factor as our final value. We also try image subtraction technique by using the r' -band image of PS1 (though the image of PS1 as template, and the resultant SN magnitude is 21.844 ± 0.086 mag, which is ~ 0.153 mag fainter than the estimate by using a scale factor of 0.45.

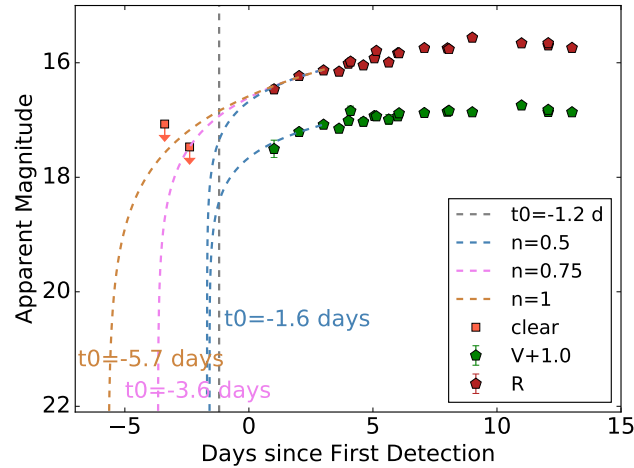


Figure A2. $A(t - t_0)^n$ fit for the first three data points of SN 2015bf. The gray dashed line represents our estimated explosion time (the midpoint between the epoch of last nondetection and discovery). The explosion time estimated by $n = 0.5$ is close to the midpoint. The expected light curve calculated by $n = 1$ (orange dashed line) is above the last nondetection, while the expected light curve calculated by $n = 0.75$ (purple dashed line) is almost pass through the last nondetection. Thus, we adopt $n = 0.75$ to estimate the earliest limit of explosion time.

Table A1. Photometric Standard Stars in the SN 2015bf Field

Num	α (J2000)	δ (J2000)	U (mag)	B (mag)	V (mag)	R (mag)	I (mag)
1	23:24:51.50	15:13:02.8	...	14.738(0.005)	14.108(0.002)	13.751(0.002)	13.326(0.002)
2	23:24:56.36	15:15:15.7	...	15.705(0.009)	14.928(0.004)	14.523(0.003)	14.062(0.003)
3	23:24:35.85	15:13:28.2	16.462(0.008)	16.406(0.018)	15.873(0.008)	15.486(0.006)	15.077(0.006)
4	23:24:48.50	15:18:15.7	...	16.576(0.020)	15.885(0.008)	15.480(0.006)	14.977(0.006)
5	23:24:43.96	15:13:38.1	17.272(0.010)	17.143(0.032)	16.459(0.014)	16.037(0.010)	15.627(0.010)
6	23:24:52.96	15:14:55.3	17.604(0.012)	17.464(0.044)	16.737(0.018)	16.415(0.014)	15.989(0.013)
7	23:24:36.14	15:15:45.5	17.713(0.014)	16.958(0.027)	16.078(0.010)	15.513(0.007)	14.981(0.007)
8	23:24:52.20	15:18:57.4	...	17.269(0.037)	16.316(0.013)	15.781(0.009)	15.147(0.007)
9	23:25:03.56	15:21:16.5	...	13.265(0.002)	12.739(0.001)	12.417(0.001)	12.031(0.001)
10	23:25:02.56	15:14:47.1	18.298(0.018)	17.226(0.026)	15.819(0.008)	14.909(0.004)	13.852(0.001)

Table A2. Clear-band Photometry of SN 2015bf

JD	Phase ^a (d)	Magnitude
2457372.60	4.83	16.51 (0.03)
2457373.58	5.81	16.38 (0.03)
2457374.60	6.83	16.40 (0.07)
2457386.60	18.83	16.26 (0.03)
2457399.60	31.83	16.45 (0.07)
2457408.62	40.85	16.73 (0.04)
2457415.62	47.85	16.86 (0.03)

^aPhase relative to the estimated explosion date.

Table A3. Optical Photometry of SN 2015bf

JD	Phase ^a (d)	<i>U</i> (mag)	<i>B</i> (mag)	<i>V</i> (mag)	<i>R</i> (mag)	<i>I</i> (mag)	Telescope
2457369.98	2.21	16.964(0.153)	16.829(0.073)	16.721(0.040)	LJT
2457370.99	3.22	...	16.649(0.019)	16.668(0.012)	16.597(0.026)	16.516(0.018)	TNT
2457371.98	4.21	...	16.605(0.012)	16.540(0.010)	16.498(0.030)	16.352(0.023)	TNT
2457372.14	4.37	15.675(0.078)	16.614(0.017)	...	16.260(0.030)	...	LJT
2457372.60	4.83	...	16.68(0.12)	16.61(0.06)	16.52(0.05)	16.32(0.06)	KAIT
2457372.98	5.21	...	16.591(0.018)	16.473(0.011)	16.380(0.023)	16.231(0.018)	TNT
2457373.07	5.30	15.612(0.091)	16.526(0.019)	16.300(0.083)	16.345(0.066)	16.068(0.061)	LJT
2457373.58	5.81	...	16.85(0.14)	16.49(0.07)	16.41(0.05)	16.26(0.06)	KAIT
2457374.03	6.26	...	16.541(0.070)	16.388(0.013)	16.286(0.023)	16.060(0.018)	TNT
2457374.11	6.34	15.557(0.060)	...	16.394(0.019)	16.157(0.051)	16.012(0.029)	LJT
2457374.61	6.84	...	16.70(0.21)	16.45(0.09)	16.36(0.07)	16.21(0.09)	KAIT
2457374.97	7.20	...	16.505(0.010)	16.394(0.013)	16.197(0.031)	16.040(0.048)	TNT
2457375.02	7.25	15.504(0.095)	16.527(0.012)	16.341(0.020)	16.198(0.047)	16.023(0.026)	LJT
2457376.04	8.27	...	16.627(0.018)	16.336(0.024)	16.109(0.046)	15.895(0.025)	LJT
2457376.97	9.20	...	16.551(0.043)	16.313(0.011)	16.113(0.034)	15.933(0.019)	TNT
2457377.03	9.26	...	16.638(0.013)	16.297(0.033)	16.127(0.050)	15.894(0.029)	LJT
2457377.97	10.20	...	16.544(0.022)	16.323(0.009)	15.926(0.064)	15.921(0.027)	TNT
2457379.96	12.19	...	16.611(0.063)	16.204(0.048)	16.025(0.040)	15.848(0.066)	TNT
2457380.06	12.29	15.371(0.172)	LJT
2457381.03	13.26	...	16.625(0.022)	16.318(0.020)	16.061(0.024)	15.843(0.016)	TNT
2457381.03	13.26	15.846(0.054)	16.609(0.022)	16.281(0.027)	16.023(0.049)	15.738(0.030)	LJT
2457381.99	14.22	...	16.721(0.060)	16.323(0.012)	16.105(0.026)	15.822(0.022)	TNT
2457382.01	14.24	16.066(0.054)	15.801(0.039)	LJT
2457384.03	16.26	15.926(0.306)	16.646(0.009)	16.326(0.040)	16.077(0.051)	15.789(0.057)	LJT
2457385.02	17.25	...	16.629(0.015)	16.332(0.010)	16.111(0.027)	15.817(0.020)	TNT
2457386.60	18.83	...	16.91(0.12)	16.45(0.05)	16.25(0.04)	15.95(0.05)	KAIT
2457388.05	20.28	...	16.769(0.010)	16.418(0.031)	16.105(0.047)	15.805(0.027)	LJT
2457389.99	22.23	...	16.984(0.029)	16.496(0.013)	16.234(0.025)	15.920(0.023)	TNT
2457390.99	23.22	...	16.987(0.021)	16.509(0.014)	16.222(0.023)	15.894(0.016)	TNT
2457391.99	24.23	16.496(0.074)	16.169(0.064)	15.899(0.045)	LJT
2457392.97	25.0	...	17.021(0.011)	16.528(0.008)	16.220(0.024)	15.952(0.016)	TNT
2457393.02	25.25	16.868(0.052)	17.011(0.014)	16.494(0.048)	16.210(0.052)	15.916(0.026)	LJT
2457393.98	26.21	...	17.107(0.015)	16.576(0.013)	16.273(0.025)	15.994(0.015)	TNT
2457394.99	27.23	...	17.165(0.013)	16.562(0.013)	16.253(0.024)	15.944(0.014)	TNT
2457395.96	28.19	...	17.338(0.077)	16.589(0.011)	16.291(0.027)	15.982(0.019)	TNT
2457396.02	28.26	17.151(0.047)	17.253(0.027)	16.606(0.060)	16.259(0.054)	15.972(0.028)	LJT
2457397.99	30.22	...	17.324(0.022)	16.654(0.015)	16.310(0.027)	16.016(0.017)	TNT
2457399.99	32.21	...	17.550(0.028)	16.701(0.013)	16.354(0.026)	16.091(0.019)	TNT
2457401.01	33.24	...	17.457(0.020)	16.785(0.017)	16.416(0.034)	16.061(0.017)	TNT
2457401.96	34.19	...	17.640(0.032)	16.697(0.018)	16.508(0.055)	16.030(0.024)	TNT
2457403.01	35.24	17.969(0.096)	17.694(0.019)	16.786(0.035)	16.376(0.052)	16.051(0.028)	LJT
2457404.99	37.22	...	17.993(0.117)	16.959(0.040)	16.522(0.042)	16.189(0.033)	TNT
2457406.97	39.20	...	18.091(0.073)	16.915(0.015)	16.564(0.101)	16.208(0.021)	TNT
2457415.63	47.86	...	17.83(0.25)	17.24(0.13)	16.78(0.08)	16.45(0.08)	KAIT
2457416.97	49.20	...	18.114(0.146)	17.245(0.089)	16.717(0.051)	16.222(0.032)	TNT
2457419.95	52.18	...	18.530(0.064)	17.353(0.030)	16.765(0.033)	16.425(0.020)	TNT
2457420.96	53.19	...	18.532(0.052)	17.357(0.022)	16.738(0.031)	16.408(0.025)	TNT
2457423.95	56.18	...	18.379(0.061)	17.434(0.034)	16.810(0.036)	16.395(0.030)	TNT
2457424.95	57.18	...	18.494(0.041)	17.464(0.033)	16.829(0.045)	16.488(0.030)	TNT
2457573.08	205.31	21.691(0.128)	...	Keck

^aPhase relative to the estimated explosion date.

Table A4. *Swift* UVOT Photometry of SN 2015bf

JD	Phase ^a (d)	Filter	Magnitude
2457370.82	3.05	<i>uvw2</i>	15.211(0.070)
2457372.20	4.43	<i>uvw2</i>	15.411(0.078)
2457373.22	5.45	<i>uvw2</i>	15.525(0.068)
2457377.18	9.41	<i>uvw2</i>	16.574(0.077)
2457377.92	10.16	<i>uvw2</i>	16.553(0.100)
2457379.10	11.33	<i>uvw2</i>	17.008(0.085)
2457380.76	12.99	<i>uvw2</i>	17.274(0.092)
2457383.32	15.55	<i>uvw2</i>	17.926(0.119)
2457384.59	16.82	<i>uvw2</i>	18.085(0.123)
2457387.08	19.31	<i>uvw2</i>	18.480(0.160)
2457370.83	3.06	<i>uvm2</i>	15.302(0.060)
2457373.22	5.45	<i>uvm2</i>	15.503(0.062)
2457377.74	9.97	<i>uvm2</i>	16.430(0.071)
2457379.11	11.34	<i>uvm2</i>	16.787(0.078)
2457380.77	13.00	<i>uvm2</i>	17.181(0.087)
2457383.33	15.56	<i>uvm2</i>	17.911(0.123)
2457384.59	16.82	<i>uvm2</i>	18.118(0.137)
2457387.09	19.32	<i>uvm2</i>	18.988(0.245)
2457370.81	3.04	<i>uvw1</i>	15.332(0.070)
2457372.22	4.45	<i>uvw1</i>	15.347(0.065)
2457377.73	9.96	<i>uvw1</i>	15.920(0.068)
2457379.10	11.33	<i>uvw1</i>	16.174(0.071)
2457380.76	12.99	<i>uvw1</i>	16.481(0.076)
2457383.32	15.55	<i>uvw1</i>	16.924(0.089)
2457384.59	16.82	<i>uvw1</i>	17.028(0.089)
2457387.08	19.31	<i>uvw1</i>	17.619(0.122)
2457370.82	3.05	<i>u</i>	15.492(0.072)
2457373.21	5.44	<i>u</i>	15.407(0.065)
2457377.16	9.40	<i>u</i>	15.602(0.060)
2457377.73	9.96	<i>u</i>	15.567(0.067)
2457379.10	11.33	<i>u</i>	15.653(0.067)
2457380.76	12.99	<i>u</i>	15.788(0.069)
2457383.32	15.55	<i>u</i>	16.015(0.073)
2457384.59	16.82	<i>u</i>	16.135(0.072)
2457387.08	19.31	<i>u</i>	16.344(0.079)
2457370.82	3.05	<i>b</i>	16.709(0.084)
2457373.22	5.45	<i>b</i>	16.673(0.073)
2457377.73	9.96	<i>b</i>	16.632(0.072)
2457379.10	11.33	<i>b</i>	16.572(0.070)
2457380.76	12.99	<i>b</i>	16.600(0.071)
2457383.32	15.55	<i>b</i>	16.679(0.073)
2457384.59	16.82	<i>b</i>	16.826(0.074)
2457387.08	19.31	<i>b</i>	16.829(0.077)
2457370.82	3.05	<i>v</i>	16.876(0.138)
2457373.22	5.45	<i>v</i>	16.473(0.094)
2457377.74	9.96	<i>v</i>	16.220(0.084)
2457379.10	11.33	<i>v</i>	16.242(0.083)
2457380.76	13.00	<i>v</i>	16.332(0.087)
2457383.32	15.55	<i>v</i>	16.398(0.091)
2457384.59	16.82	<i>v</i>	16.410(0.088)
2457387.08	19.31	<i>v</i>	16.439(0.095)

^aPhase relative to the estimated explosion date.

Table A5. Log of Spectroscopic Observations of SN 2015bf

UT Date	JD	Phase ^a (d)	Telescope	Instrument	Range (Å)
2015/12/13	2457369.99	2.2	LJT	YFOSC+G3	3450–8830
2015/12/16	2457373.08	5.3	LJT	YFOSC+G14	3760–7450
2015/12/17	2457373.60	5.8	Lick 3 m	Kast	3400–10,300
2015/12/17	2457373.93	6.2	Xinglong 2.16 m	OMR	3700–8360
2015/12/18	2457374.99	7.2	LJT	YFOSC+G3	3460–8830
2015/12/19	2457376.01	8.2	LJT	YFOSC+G3	3460–8830
2015/12/21	2457378.10	10.3	LJT	YFOSC+G3	3440–8830
2015/12/31	2457388.05	20.3	LJT	YFOSC+G3	3450–8830
2016/01/05	2457393.02	25.2	LJT	YFOSC+G3	3450–8830
2016/01/07	2457394.50	26.7	Keck-II	DEIMOS	4490–9450
2016/01/08	2457396.03	28.3	LJT	YFOSC+G3	2440–8840
2016/01/10	2457397.99	30.2	Xinglong 2.16 m	BFOSC	3710–8640
2016/01/15	2457402.99	35.2	LJT	YFOSC+G3	3450–8840
2016/01/30	2457418.01	50.2	LJT	YFOSC+G3	3440–8830
2016/07/03	2457572.50	204.7	Keck-I	LRIS	3440–10,100

^aPhase relative to the estimated explosion date.